

# SCALE: Scalable Conditional Atlas-Level Endpoint transport for virtual cell perturbation prediction

Shuizhou Chen<sup>1,2</sup> ♣, Lang Yu<sup>1,4</sup> ♣, Kedu Jin<sup>1,3</sup>, Songming Zhang<sup>1,5</sup>, Hao Wu<sup>1</sup>, Wenxuan Huang<sup>1</sup>, Sheng Xu<sup>1</sup>, Quan Qian<sup>2</sup> ♣, Qin Chen<sup>4</sup> ♣, Lei Bai<sup>1</sup> ♣, Siqi Sun<sup>1</sup> ♣ and Zhangyang Gao<sup>1</sup> ♣

<sup>1</sup>Shanghai Artificial Intelligence Laboratory, <sup>2</sup>School of Computer Engineering & Science, Shanghai University, <sup>3</sup>School of Life Science and Technology, China Pharmaceutical University, <sup>4</sup>School of Computer Science and Technology, East China Normal University, <sup>5</sup>Faculty of Computer Science and Control Engineering, Shenzhen University of Advanced Technology, Shenzhen

Virtual cell models aim to enable *in silico* experimentation by predicting how cells respond to genetic, chemical, or cytokine perturbations from single-cell measurements. In practice, however, large-scale perturbation prediction remains constrained by three coupled bottlenecks: inefficient training and inference pipelines, unstable modeling in high-dimensional sparse expression space, and evaluation protocols that overemphasize reconstruction-like accuracy while underestimating biological fidelity. In this work we present a specialized large-scale foundation model SCALE for virtual cell perturbation prediction that addresses the above limitations jointly. First, we build a BioNeMo-based training and inference framework that substantially improves data throughput, distributed scalability, and deployment efficiency, yielding  $12.51\times$  speedup on pretrain and  $1.29\times$  on inference over the prior SOTA pipeline under matched system settings. Second, we formulate perturbation prediction as conditional transport and implement it with a set-aware flow architecture that couples LLaMA-based cellular encoding with endpoint-oriented supervision. This design yields more stable training and stronger recovery of perturbation effects. Third, we evaluate the model on Tahoe-100M using a rigorous cell-level protocol centered on biologically meaningful metrics rather than reconstruction alone. On this benchmark, our model improves PDCorr by 12.02% and DE Overlap by 10.66% over STATE. Together, these results suggest that advancing virtual cells requires not only better generative objectives, but also the co-design of scalable infrastructure, stable transport modeling, and biologically faithful evaluation.

## 1. Introduction

Virtual cell models aim to turn single-cell perturbation data into *in silico* systems for forecasting how cellular states respond to genetic, chemical or cytokine interventions[1, 2]. Such models could accelerate hypothesis generation and mechanism-oriented screening by enabling candidate perturbations to be evaluated before costly wet-lab experiments[3, 4]. In this context, perturbation prediction is not simply a benchmark task but a foundational ability for any useful virtual cell system: the model must faithfully capture how cellular populations reorganize under intervention[3, 5].

Perturbation prediction from single-cell data is intrinsically difficult because the same cell cannot be observed both before and after intervention. The task is therefore not to reconstruct paired cell-level trajectories, but to infer how an untreated population is redistributed under perturbation. This population-level inference is challenging in single-cell transcriptomic space, which is high-dimensional, sparse and biologically heterogeneous, while also being shaped by substantial technical variation across batches and experimental contexts. As perturbation atlases continue to expand in scale and diversity, these difficulties become more pronounced, creating a need for methods that remain computationally tractable, learn stable population-level state transitions and are evaluated with metrics that reflect biological fidelity rather than average expression reconstruction alone.

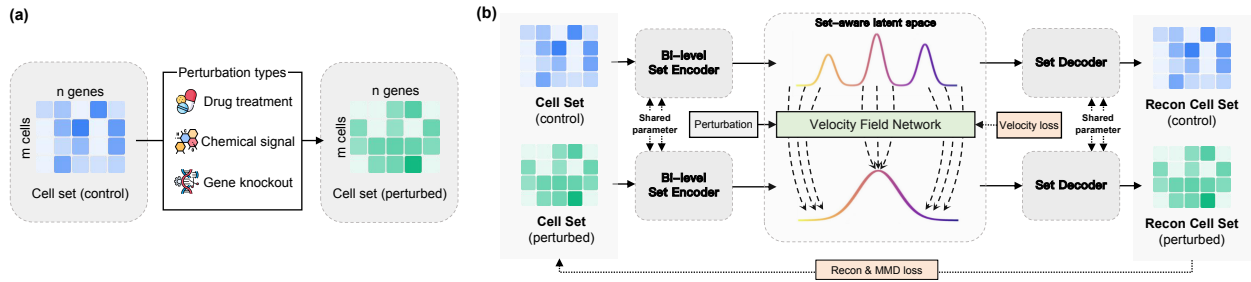


Figure 1 | **Overview of SCALE.** (a) **Conceptual formulation of virtual cell perturbation prediction.** Given control and perturbed single-cell populations measured under matched biological context, the task is framed as conditional transport from control to perturbed cell states. Rather than assuming one-to-one correspondence between cells, the model learns population-level perturbation-induced transitions over unordered cellular sets. (b) **SCALE for scalable and biologically faithful perturbation prediction.** SCALE encodes cellular populations into a set-aware latent space and learns stable endpoint-aligned transport under perturbation conditions. This design is coupled with scalable training infrastructure and biologically grounded evaluation to support large-scale virtual cell modeling.

Existing methods have made important progress, but key limitations remain. Early approaches often relied on direct conditional mapping or randomly paired regression, which tend to emphasize average perturbation effects and can miss heterogeneous cellular responses. More recent methods instead shift the objective from cell-level matching to population-level prediction: STATE highlights the importance of heterogeneity-aware set modeling and biologically grounded evaluation, whereas PerturbDiff suggests that an observed perturbation may correspond to a family of plausible response distributions shaped by unobserved latent factors. These advances broaden the modeling perspective, but they still largely rely on two-stage formulations that separate latent representation learning from perturbation generation. This creates a key mismatch: latent spaces optimized for reconstruction are not necessarily suited to modeling perturbation-induced population shifts, and may even become trivial or overly instance-preserving. What is needed instead is an end-to-end formulation that jointly learns set-level representations and perturbation-conditioned state transitions.

In this work, we propose SCALE, a large-scale foundation model built around an end-to-end formulation that jointly learns set-level representations and perturbation-conditioned state transitions. SCALE instantiates this formulation with a LLaMA-style set encoder and a conditional flow-matching architecture, enabling stable prediction of perturbation-induced population shifts in sparse, high-dimensional single-cell space. To support atlas-scale training and deployment, we further implement the model within a BioNeMo-based framework for high-throughput data processing, distributed execution and efficient inference on Tahoe-100M.

We evaluate SCALE using a rigorous cell-level protocol centered on biologically meaningful recovery over multiple perturbation datasets. On Tahoe-100M, our model improves PDCorr by 12.02% and DE Overlap by 10.66% over STATE, indicating gains not only in expression prediction but also in the recovery of perturbation effects. These results support a broader conclusion: progress in virtual cell modeling depends not only on more expressive generative objectives, but on the co-design of scalable systems, stable transport modeling, and biologically faithful evaluation.

Our contributions are threefold:

- **Scalable virtual-cell infrastructure.** We develop a BioNeMo-based pretraining and inference framework for virtual cell perturbation prediction, meanwhile a new sampling strategy for the perturb dataset, making atlas-scale model development practical and delivering nearly  $12.51\times$

speedup over the prior SOTA pipeline STATE under matched system settings.

- **Endpoint-aligned conditional transport for perturbation prediction.** We formulate single-cell perturbation prediction as conditional transport between control and perturbed cellular populations in a learned set-aware latent space, and instantiate it with a LLaMA-style DeepSets encoder and JiT parameterization [6] under paired endpoint supervision. This formulation is designed to better match the supervision actually available in perturbation datasets, where only the initial and final population states are observed.
- **Meaningful gains on biologically grounded metrics.** Under rigorous cell-level evaluation on Tahoe-100M, SCALE improves *PDCorr* by 12.02% and *DE Overlap* by 10.66% over STATE, showing that the gains arise not only from better expression fitting, but from stronger recovery of perturbation effects on biologically grounded metrics.

## 2. Related Work

**Single-cell foundation models for virtual cell.** Recent progress in large-scale single-cell foundation models [7–9] has accelerated the development of virtual cells as *in silico* systems for biological experimentation. Models such as scGPT [8] demonstrate that atlas-scale pretraining can produce transferable representations for cellular analysis. However, perturbation prediction imposes a stricter requirement than representation learning alone: a useful virtual cell model must predict how cellular states change under intervention across heterogeneous biological and experimental contexts.

**Direct conditional mapping for virtual cell.** A substantial line of prior work [10–14] formulates perturbation prediction as a direct conditional mapping from control cells to perturbed outcomes. scGen [10] models perturbational effects as latent shifts in a variational framework, CPA [11] extends this paradigm to compositional perturbations and covariates, and GEARS [12] incorporates gene–gene interaction structure to improve prediction for unseen multi-gene perturbations. These methods established strong and computationally efficient baselines for the field. Nevertheless, because single-cell perturbation data are inherently unpaired, direct cell-wise objectives can bias learning toward average effects, making it difficult to recover heterogeneous population-level responses. This limitation is underscored by recent benchmarking work showing that current deep perturbation models do not yet consistently surpass strong linear baselines across settings [15].

**Population-level perturbation models for virtual cell.** To address the limitations of random pairing and mean-effect regression, a more recent family of methods [4, 16–21] model perturbation responses at the level of populations, sets, or transport maps. CellOT [16] frames perturbation prediction through neural optimal transport between control and perturbed populations. STATE [22] extends this direction with transformer-based set modeling, emphasizing heterogeneity-aware prediction across sets of cells and evaluating models with biologically grounded cell-level metrics. Diffusion-based approaches such as scPPDM [23] further extend this paradigm. PerturbDiff [24] pushes the formulation further by treating cell distributions as random variables and defining diffusion directly in RKHS, thereby modeling response variability induced by unobserved latent factors. Closely related recent work has also explored continuous-time or bridge-based generative formulations, including CellFlow [25] and Unlasting [26].

**Positioning of SCALE.** Our work is most closely related to this last family of population and transport-oriented methods, but differs in emphasis. Compared with direct mapping methods, we explicitly formulate perturbation prediction as conditional transport rather than one-shot regression. Compared with set-based approaches such as STATE, we place greater emphasis on latent transport

learning as the modeling primitive. Compared with distribution-level diffusion approaches such as PerturbDiff, our focus is not only on expressive generative modeling, but on a practical atlas-scale framework that couples scalable infrastructure, stable and efficient perturbation transport learning, and performance gains on biologically grounded metrics.

### 3. SCALE

#### 3.1. Problem Formulation

We study single-cell perturbation prediction from paired *cell-level* observations. Each training sample consists of a control cell set  $X_0$ , a perturbed cell set  $X_1$ , and a collection of observed conditions, including celltype  $c$ , perturbation identity  $p$ , and experimental batch  $b$ :

$$\mathcal{D} = \{(X_0, X_1, c, p, b)\}. \quad (1)$$

Here  $X_0, X_1 \in \mathbb{R}^{B \times N \times G}$  denote batches of cell sets, where  $B$  is the batch size,  $N$  is the number of cells sampled per example, and  $G$  is the number of genes. Within each example, cells are treated as an unordered set rather than a sequence.

The key difficulty is that single-cell perturbation measurements are inherently unpaired: the same cell cannot be observed both before and after treatments. Therefore, the goal is not to learn a one-to-one cell correspondence, but to model how a control population is redistributed under perturbation. Formally, we seek to learn the conditional law

$$\hat{X}_1 \sim p_\theta(X_1 | X_0, c, p, b), \quad (2)$$

where the prediction target is the post-perturbation population conditioned on the pre-perturbation population and observed metadata.

This perspective places perturbation prediction closer to a *conditional population transport* problem than to standard cell-wise regression. The model must preserve perturbation-relevant variation across cells while transforming the control population into a perturbed one under context-specific constraints. This is particularly challenging in transcriptomic space, which is high-dimensional, sparse, and noisy, making direct transport learning in the observed space difficult to optimize. The detailed module of our model can be seen in Figure 2.

#### 3.2. A Hierarchical Set-Aware Latent Cell-State Encoder

To make conditional transport tractable and stable while preserving distribution-level observations, we construct a hierarchical latent encoder rather than a generic cell-wise autoencoder. The key observation is that each training example is an unordered set of cells, while each cell itself is a high-dimensional gene-expression object. This motivates a two-level factorization of representation learning: we first model *within-cell* gene dependencies, and then model *across-cell* distribution.

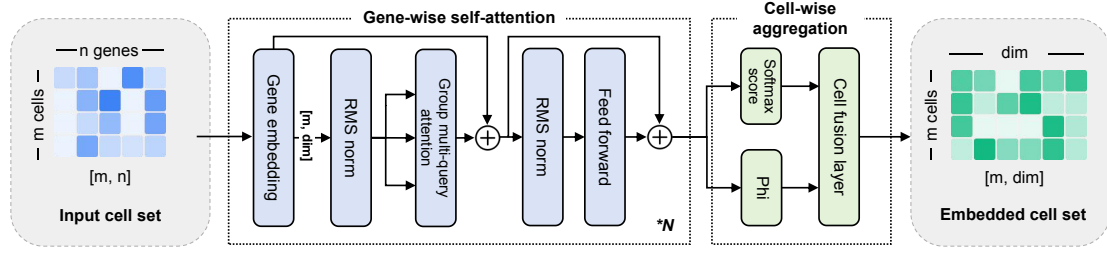
**Gene-wise encoding within each cell.** Let  $x_i \in \mathbb{R}^G$  denote the expression vector of the  $i$ -th cell in a population. We first apply a shared gene-wise encoder

$$f_{\text{gene}} : \mathbb{R}^G \rightarrow \mathbb{R}^d, \quad (3)$$

to each cell independently, yielding

$$h_i = f_{\text{gene}}(x_i), \quad i = 1, \dots, N. \quad (4)$$

(a) Hierarchical Set-Aware encoder



(b) Conditional JiT-based velocity field network

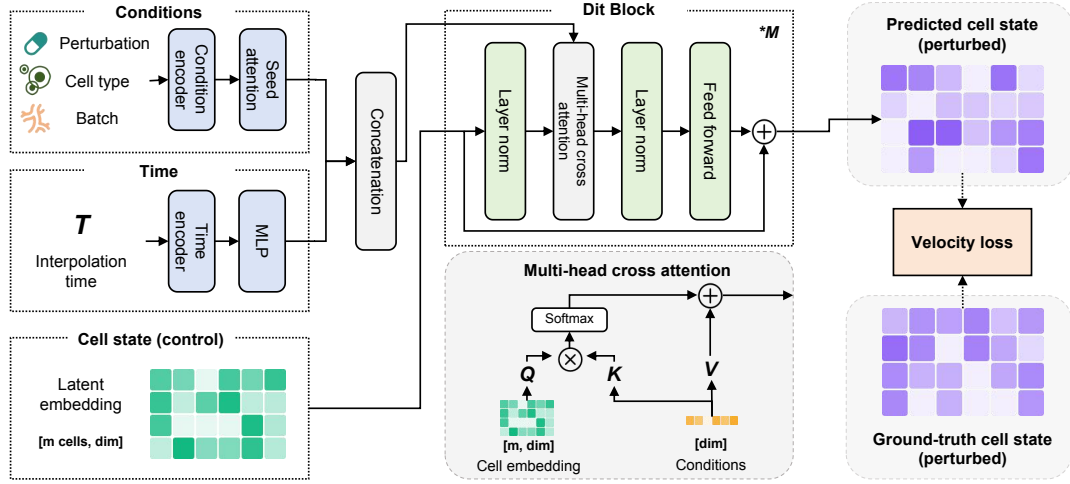


Figure 2 | **SCALE module detail.** (a) **Hierarchical set-aware encoder.** This module firstly encodes gene-level cell inputs into latent cell embeddings through stacked set-transformer blocks and aggregate the cell-wise information with a set equivariant fusion layer. (b) **Conditional JiT-based velocity field network.** This module integrates condition features, time encoding, and cell latent embeddings to model perturbation latent transportation and predict target embeddings through velocity fitting.

In our implementation,  $f_{\text{gene}}$  is instantiated as a LLaMA-style attention or a basic attention module operating over gene-level features *within* a single cell. Importantly, this stage does not perform cell-to-cell interaction: the same encoder is applied independently to every cell. As a result, with respect to permutations of cell order, this stage is naturally permutation equivariant:

$$F_{\text{gene}}(PX) = PF_{\text{gene}}(X), \quad (5)$$

where  $X \in \mathbb{R}^{B \times N \times G}$  is a batch of cell sets,  $P$  is a permutation acting on the cell dimension, and  $F_{\text{gene}}(X)$  returns cell-wise embeddings. For the  $b$ -th cell set, let

$$H^{(b)} = [h_1^{(b)}, \dots, h_N^{(b)}] \in \mathbb{R}^{N \times d_h}, \quad (6)$$

where  $h_i^{(b)} \in \mathbb{R}^{d_h}$  denotes the gene-level embedding of the  $i$ -th cell. For notational simplicity, we omit the batch index  $b$  below and write  $h_i \in \mathbb{R}^{d_h}$ .

**DeepSets aggregation across cells.** The cell embeddings are then processed at the population level through a DeepSets layer over the cell dimension. Specifically, we compute a permutation-invariant

population summary

$$s(X) = \rho \left( \frac{1}{N} \sum_{i=1}^N \phi(h_i) \right) \in \mathbb{R}^{d_s}, \quad (7)$$

where  $\phi : \mathbb{R}^{d_h} \rightarrow \mathbb{R}^{d_\phi}$  and  $\rho : \mathbb{R}^{d_\phi} \rightarrow \mathbb{R}^{d_s}$  are learnable mappings. In batched form, stacking the set-level summaries across the  $B$  samples yields  $S(X) \in \mathbb{R}^{B \times d_s}$ .

This summary is then fed back to refine each cell representation through a learnable fusion map

$$z_i = \psi(h_i, s(X)), \quad \psi : \mathbb{R}^{d_h} \times \mathbb{R}^{d_s} \rightarrow \mathbb{R}^d, \quad i = 1, \dots, N, \quad (8)$$

so that  $z_i \in \mathbb{R}^d$ . Stacking the refined cell embeddings gives the final latent population

$$Z = [z_1, \dots, z_N] \in \mathbb{R}^{N \times d}, \quad (9)$$

and, in batched form,  $Z \in \mathbb{R}^{B \times N \times d}$ .

By construction,  $s(X)$  is permutation invariant, while the refined cell representations remain permutation equivariant with respect to any reordering of the input cells. In this way, the encoder faithfully preserves the intrinsic symmetry structure of unordered cell sets, while still allowing informative global population-level context to modulate and enrich each individual cell embedding.

**Interpretation.** This hierarchical encoder separates two distinct modeling roles. The LLaMA-style gene encoder captures intracellular transcriptional dependencies, whereas the DeepSets layer captures population-level structure across cells. Therefore, the latent representation is not merely a dimension-reduced cell embedding, but a *set-aware latent population representation* that respects both the internal structure of each cell and the unordered structure of the cell population.

**Autoencoding objective.** Let the full encoder and decoder be denoted by

$$Enc_\phi : \mathbb{R}^{B \times N \times G} \rightarrow \mathbb{R}^{B \times N \times d}, \quad Dec_\psi : \mathbb{R}^{B \times N \times d} \rightarrow \mathbb{R}^{B \times N \times G}, \quad (10)$$

where  $Enc_\phi$  denotes the hierarchical encoder described above, operating on  $B$  batch of cell sets of size  $N$  with  $G$  genes per cell. In batched form, the inputs and outputs are stacked over the batch dimension.

Applied to the control and perturbed populations, we obtain

$$Z_0 = Enc_\phi(X_0), \quad Z_1 = Enc_\phi(X_1), \quad Z_0, Z_1 \in \mathbb{R}^{B \times N \times d}, \quad (11)$$

where  $X_0, X_1 \in \mathbb{R}^{B \times N \times G}$ .

The decoder reconstructs expression cell-wise,

$$\hat{X}_0 = Dec_\psi(Z_0), \quad \hat{X}_1 = Dec_\psi(Z_1), \quad \hat{X}_0, \hat{X}_1 \in \mathbb{R}^{B \times N \times G}. \quad (12)$$

To encourage both point-wise reconstruction fidelity and population-level distribution alignment, we train the latent space with a joint MSE-MMD objective:

$$\mathcal{L}_{AE} = \mathcal{L}_{MSE} + \lambda_{MMD} \mathcal{L}_{MMD}, \quad (13)$$

where

$$\mathcal{L}_{MSE} = \mathbb{E}_{X_0} \left[ \|\hat{X}_0 - X_0\|_2^2 \right] + \mathbb{E}_{X_1} \left[ \|\hat{X}_1 - X_1\|_2^2 \right], \quad (14)$$

$$\mathcal{L}_{MMD} = \mathbb{E} \left[ \text{MMD}^2(\hat{X}_0, X_0) \right] + \mathbb{E} \left[ \text{MMD}^2(\hat{X}_1, X_1) \right]. \quad (15)$$

Here,  $\lambda_{\text{MMD}}$  balances local reconstruction accuracy and global distribution matching. The MMD term is defined as

$$\text{MMD}^2(A, B) = \mathbb{E}_{a, a' \sim A}[k(a, a')] + \mathbb{E}_{b, b' \sim B}[k(b, b')] - 2\mathbb{E}_{a \sim A, b \sim B}[k(a, b)], \quad (16)$$

where  $k(\cdot, \cdot)$  is a positive-definite kernel, e.g., a Gaussian kernel.

### 3.3. Conditional Latent Flow Transport under Paired Endpoint Supervision

Because training data provide paired control and perturbed cell sets but do not reveal the intermediate transition trajectory, we formulate perturbation prediction as conditional latent transport between two observed endpoints rather than as reconstruction of a full stochastic reverse process. Let

$$Z_0 = \text{Enc}_\phi(X_0), \quad Z_1 = \text{Enc}_\phi(X_1), \quad Z_0, Z_1 \in \mathbb{R}^{B \times N \times d} \quad (17)$$

denote the set-aware latent populations encoded from the control and perturbed cell sets. We connect the two endpoints through a simple linear surrogate path

$$Z_t = (1 - t)Z_0 + tZ_1, \quad t \sim \text{Uniform}(0, 1), \quad (18)$$

which serves as an observation-compatible training construction rather than a literal model of biological dynamics. Here,  $t$  is a scalar interpolation time sampled uniformly from the unit interval.

Given the interpolated latent distribution  $Z_t$ , time  $t$ , and observed conditions  $C$ , the conditional transport backbone produces hidden latent states

$$H_t = g_\theta(Z_t, t, C), \quad H_t \in \mathbb{R}^{B \times N \times d}. \quad (19)$$

Here,  $g_\theta(\cdot)$  is the conditional transport flow model parameterized by  $\theta$ . The final SCALE model is instantiated through direct prediction head:

$$\hat{Z}_1 = h_x(H_t), \quad (20)$$

where  $h_x(\cdot)$  is the endpoint prediction head and  $\hat{Z}_1$  is the predicted perturbed latent population, and is trained with the endpoint reconstruction objective

$$\mathcal{L}_{\text{flow}} = \mathcal{L}_x = \mathbb{E}_t \left[ \|\hat{Z}_1 - Z_1\|_2^2 \right]. \quad (21)$$

Here,  $\mathbb{E}_t[\cdot]$  denotes expectation over the sampled interpolation time  $t$ . It is obvious that we adopt JiT x-pred and x-loss training strategy.

This endpoint-oriented formulation matches the supervision available in single-cell perturbation prediction. During training, we observe the control population and the perturbed population only at the endpoints, while the intermediate continuous transition is unobserved. Therefore, supervising the predicted perturbed endpoint provides the most faithful way to align the learning objective with the data actually available during training.

**JiT parameterization family.** Beyond the final deployed objective, we consider a broader JiT [6] parameterization family to analyze how the choice of prediction target affects optimization and final-state recovery. In particular, JiT includes both endpoint-style and velocity/displacement-style parameterizations derived from the same latent transport framework. These variants are introduced for ablation and analysis rather than deployment, with the goal of isolating how the choice of prediction target and supervision space affects training under paired endpoint supervision.

Let the endpoint and displacement heads be denoted by

$$\hat{Z}_1 = h_x(H_t), \quad (22)$$

$$\hat{U} = h_v(H_t), \quad (23)$$

where  $h_v(\cdot)$  is the displacement prediction head and  $\hat{U}$  is the predicted latent displacement, with the corresponding conversion

$$\hat{Z}_1 = Z_0 + \hat{U}, \quad \hat{U} = \hat{Z}_1 - Z_0. \quad (24)$$

We further define the endpoint and displacement supervision spaces abstractly as

$$\mathcal{L}_x = \mathbb{E}_t \left[ \|\hat{Z}_1 - Z_1\|_2^2 \right], \quad (25)$$

$$\mathcal{L}_v = \mathbb{E}_t \left[ \|\hat{U} - U^*\|_2^2 \right], \quad (26)$$

where  $U^* = Z_1 - Z_0$  denotes the ground-truth latent displacement, which yield four JiT variants:

$$x\text{-pred} / x\text{-loss}: \quad \hat{Z}_1 = h_x(H_t), \quad \mathcal{L} = \mathcal{L}_x, \quad (27)$$

$$x\text{-pred} / v\text{-loss}: \quad \hat{Z}_1 = h_x(H_t), \quad \hat{U} = \hat{Z}_1 - Z_0, \quad \mathcal{L} = \mathcal{L}_v, \quad (28)$$

$$v\text{-pred} / x\text{-loss}: \quad \hat{U} = h_v(H_t), \quad \hat{Z}_1 = Z_0 + \hat{U}, \quad \mathcal{L} = \mathcal{L}_x, \quad (29)$$

$$v\text{-pred} / v\text{-loss}: \quad \hat{U} = h_v(H_t), \quad \mathcal{L} = \mathcal{L}_v. \quad (30)$$

These variants are studied to understand how the exposure of endpoint-versus displacement-style supervision affects optimization. Empirically, the choice of parameterization is not neutral: JiT variants substantially outperform the base flow formulation, and among the completed configurations, endpoint prediction with endpoint supervision gives the strongest results in our setting. We therefore adopt x-pred/x-loss as the default configuration of SCALE unless otherwise stated, while reporting the broader JiT comparison separately in the ablation study.

**Practical implication.** A flow-based formulation is therefore natural in our setting. Rather than reconstructing an unobserved latent stochastic process, the model learns conditional transport between supervised endpoints. The objective is thus defined on endpoint quantities available during training and aligns more naturally with endpoint-based evaluation.

### 3.4. Conditioning representation and injection

We condition on three discrete variables: cell type  $c$ , perturbation type  $p$ , and batch type  $b$ . Each condition is represented as a one-hot vector:

$$\mathbf{c} \in \{0, 1\}^{K_c}, \quad \mathbf{p} \in \{0, 1\}^{K_p}, \quad \mathbf{b} \in \{0, 1\}^{K_b}$$

where  $K_c$ ,  $K_p$ , and  $K_b$  are the numbers of cell types, perturbation types, and batch types.

**Condition embedding.** We map each one-hot vector to a dense embedding using a linear projection:

$$e_c = \mathbf{c}W_c \in \mathbb{R}^{B \times d_c}, \quad e_p = \mathbf{p}W_p \in \mathbb{R}^{B \times d_c}, \quad e_b = \mathbf{b}W_b \in \mathbb{R}^{B \times d_c},$$

with  $W_c \in \mathbb{R}^{K_c \times d_c}$ ,  $W_p \in \mathbb{R}^{K_p \times d_c}$ , and  $W_b \in \mathbb{R}^{K_b \times d_c}$ . We stack the three embeddings into a token matrix:

$$C = [e_c; e_p; e_b] \in \mathbb{R}^{B \times 3 \times d_c}.$$

**Condition injection by seed attention.** Let  $H_\ell \in \mathbb{R}^{B \times N \times d}$  denote the latent cell tokens at transformer block  $\ell$ . We first project the condition tokens into the model width,

$$\tilde{C} = \Pi(C) \in \mathbb{R}^{B \times 3 \times d}, \quad (31)$$

where  $\Pi : \mathbb{R}^{B \times 3 \times d_c} \rightarrow \mathbb{R}^{B \times 3 \times d}$  is a learned linear projection. Instead of directly concatenating all condition tokens with the cell tokens, we aggregate them into a single condition summary by a learnable seed query. Specifically, let  $q_{\text{seed}} \in \mathbb{R}^d$  be a learned seed vector. We compute

$$\alpha = \text{Softmax}\left(\frac{(q_{\text{seed}}W_Q)(\tilde{C}W_K)^\top}{\sqrt{d}}\right) \in \mathbb{R}^{B \times 1 \times 3}, \quad (32)$$

and form the aggregated condition token

$$c_{\text{seed}} = \alpha(\tilde{C}W_V) \in \mathbb{R}^{B \times 1 \times d}. \quad (33)$$

We then inject this seed-aggregated condition token by concatenating it with the cell tokens and applying standard self-attention over the joint sequence:

$$\tilde{H}_\ell = [H_\ell; c_{\text{seed}}] \in \mathbb{R}^{B \times (N+1) \times d}, \quad (34)$$

followed by the transformer update

$$\tilde{H}_{\ell+1} = \tilde{H}_\ell + \text{Attn}(\text{LN}(\tilde{H}_\ell)) + \text{MLP}(\text{LN}(\tilde{H}_\ell)). \quad (35)$$

After the update, we retain only the first  $N$  cell tokens as the latent state for the next block:

$$H_{\ell+1} = \tilde{H}_{\ell+1}[:, 1:N, :] \in \mathbb{R}^{B \times N \times d}. \quad (36)$$

Because no positional encoding is applied on the cell dimension and all token-wise parameters are shared across cells, this operation preserves permutation equivariance with respect to the cell token order, while allowing the model to inject an adaptively aggregated condition representation.

### 3.5. Generation in expression space

Given a control set  $X_0$  together with observed condition variables  $(c, p, b)$ , we first compute the latent control population  $Z_0 = \text{Enc}_\phi(X_0)$ . We then apply the trained conditional transport backbone under the chosen JiT parameterization to obtain a predicted perturbed latent population  $\hat{Z}_1$ , and decode it back to expression space:

$$\hat{X}_1 = \text{Dec}_\psi(\hat{Z}_1). \quad (37)$$

This yields a deterministic prediction of the post-perturbation population in expression space under the observed biological context.

## 4. Experiments

To comprehensively assess the capabilities of SCALE, we conduct experiments on a diverse set of challenging benchmarks.

## 4.1. Experiments Setup

**Evaluation Benchmarks.** We evaluate SCALE on three representative single-cell perturbation benchmarks spanning complementary biological regimes: PBMC for cytokine signaling perturbation prediction, Tahoe-100M for chemical perturbation prediction, and Replogle-Nadig for genetic perturbation prediction. Following the current unified pipeline, all models are trained to predict log-expression on the top 2,000 highly variable genes (HVGs), which serves as a standardized feature space across datasets [22, 24].

- **PBMC:** a large-scale cytokine perturbation benchmark built from peripheral blood mononuclear cells collected from 12 donors, comprising 90 cytokine perturbation conditions across 18 cell types. Compared with drug and genetic perturbation benchmarks, PBMC provides a dense signaling-response setting with substantial donor- and cell-type-dependent heterogeneity, making it a useful testbed for context generalization under immune stimulation [22, 24].
- **Tahoe-100M:** a large-scale chemical perturbation benchmark comprising more than 100 million single-cell expression profiles collected from 50 diverse cancer cell lines under over 1,100 treatment conditions involving hundreds of small-molecule perturbations. Its scale and cellular-context diversity make it a challenging testbed for evaluating context generalization under broad chemical intervention regimes [27].
- **Replogle-Nadig:** a large-scale genetic perturbation benchmark built from genome-scale CRISPRi Perturb-seq experiments across four human cell lines, with 2,024 genetic perturbations retained after filtering perturbations with low on-target efficacy. Compared with large-effect chemical perturbations, this benchmark is particularly useful for assessing performance on subtler transcriptomic perturbation signals [28, 29].

**Preprocessing and data splits.** For PBMC and Tahoe-100M, we follow the preprocessing protocol adopted in recent standardized benchmarks: raw count matrices are first normalized by per-cell library size, then transformed with  $\log(1 + x)$ , and finally rescaled by a constant factor of 10 before HVG selection [24]. After preprocessing, we extract the top 2,000 HVGs using the standard Scanpy pipeline for downstream prediction [24]. For Replogle-Nadig, we follow STATE’s processed release: filtering by on-target knockdown efficacy, library-size normalization, log transformation, and the same constant rescaling, then restricting the task to the shared 2,000-HVG space [22, 24].

To evaluate out-of-context generalization, we adopt dataset-specific holdout strategies. For PBMC, 4 of the 12 donors are held out for testing. To assess prediction under partial perturbation coverage, 30% of perturbations from the held-out donors are moved into the training set, while the remaining 70% are reserved for test evaluation [22, 24]. For Tahoe-100M, five phenotypically distinct cell lines are selected as a held-out test set based on PCA of pseudobulked expression profiles, and no data from these cell lines is used during model development. For Replogle-Nadig, following the standardized evaluation protocol, one cell line is held out as the test context while the remaining three cell lines are used for training and validation, together with a partial perturbation subset from the held-out context to evaluate cross-context transfer under incomplete perturbation coverage [22, 24].

## 4.2. Experimental Results

**SCALE achieves state-of-the-art performance for most of the metrics.** Firstly, we align the published STATE benchmark metrics with our internal evaluation as follows: *PR-Recall* as *DE Precise*, *FC Spearman* as *DE Spearman fold change*, and *DE Overlap Accuracy* as *DE Overlap*. For consistency with this evaluation table, all results are displayed with three-decimal precision. For benchmark baselines, we transcribed from the published PerturbDiff eval result with the Cell Eval besides the

STATE model. The results are presented in Table 1.

Table 1 | **Benchmark for few-shot results on Tahoe-100M, PBMC and Replogle datasets under the Cell Eval metric protocol.** Rows marked by † denote results reproduced in our implementation; all unmarked results are taken from PerturbDiff. Specifically, SCALE results on Tahoe-100M, PBMC and Replogle, together with STATE results on Tahoe-100M and Replogle, are reproduced in our implementation. The best result in each metric within each dataset is highlighted in bold, and the second-best result is underlined.

Model	MSE ↓	MAE ↓	PDCorr ↑	DEOver ↑	DEPrec ↑	LFCspear ↑	DirAgr ↑
<i>Tahoe-100M</i>							
SCALE ( <i>ours</i> ) <sup>†</sup>	<b>0.0002</b>	<b>0.006</b>	<b>0.953</b>	<b>0.806</b>	<b>0.765</b>	<b>0.876</b>	<b>0.949</b>
STATE <sup>†</sup> [22]	0.0006	0.036	<u>0.850</u>	<u>0.728</u>	<u>0.698</u>	<u>0.851</u>	<u>0.918</u>
PerturbDiff [24]	0.0006	0.012	<u>0.686</u>	<u>0.522</u>	<u>0.572</u>	0.445	<u>0.734</u>
Mean	0.0031	0.026	0.205	0.430	0.504	0.280	0.595
CPA [11]	0.0009	0.011	0.425	0.502	0.504	0.466	0.710
Linear	<u>0.0004</u>	<u>0.009</u>	0.723	0.505	0.576	0.514	0.760
CellFlow [25]	<u>0.0031</u>	<u>0.027</u>	0.269	0.183	0.313	0.298	0.638
Squidiff [30]	5.6270	2.244	0.011	0.420	0.581	0.276	0.501
Mean Variant (per Cell Type)	0.0007	0.010	0.461	0.504	0.508	0.578	0.688
Mean Variant (per Batch)	0.0031	0.026	0.185	0.427	0.504	0.270	0.587
Mean Variant (Overall)	0.0031	0.026	0.193	0.429	0.504	0.275	0.591
<i>PBMC</i>							
SCALE ( <i>ours</i> ) <sup>†</sup>	0.0320	0.118	<b>0.979</b>	<b>0.810</b>	<b>0.831</b>	0.516	0.682
STATE [22]	<b>1.41e-4</b>	<b>0.005</b>	0.796	0.512	0.547	<b>0.602</b>	<b>0.789</b>
PerturbDiff [24]	<u>1.91e-4</u>	<u>0.006</u>	<u>0.816</u>	<u>0.564</u>	<u>0.581</u>	<u>0.519</u>	<u>0.751</u>
Mean	8.49e-4	0.013	0.642	<u>0.564</u>	0.544	0.478	0.740
CPA [11]	1.10e-2	0.052	0.181	0.488	0.515	0.369	0.539
Linear	4.44e-4	0.009	0.646	0.549	0.581	0.366	0.666
CellFlow [25]	3.58e-4	0.009	0.628	0.270	0.350	0.377	0.652
Squidiff [30]	4.387	2.062	0.033	0.359	0.547	0.022	0.379
Mean Variant (per Cell Type)	6.39e-4	0.009	0.400	0.506	0.542	0.247	0.635
Mean Variant (per Batch)	5.59e-4	0.007	0.517	0.554	0.542	0.489	0.727
Mean Variant (Overall)	1.01e-3	0.013	0.408	0.557	0.542	0.250	0.656
<i>Replogle</i>							
SCALE ( <i>ours</i> ) <sup>†</sup>	0.0009	0.072	<b>0.909</b>	<b>0.601</b>	<b>0.345</b>	<b>0.871</b>	<b>0.979</b>
STATE <sup>†</sup> [22]	<b>0.0064</b>	<u>0.055</u>	<u>0.437</u>	<u>0.196</u>	<u>0.193</u>	<u>0.506</u>	<u>0.778</u>
PerturbDiff [24]	0.0147	<u>0.081</u>	<u>0.340</u>	<u>0.190</u>	<u>0.174</u>	<u>0.342</u>	<u>0.702</u>
Mean	0.0990	0.206	0.048	0.127	0.094	0.077	0.532
CPA [11]	0.0750	<b>0.054</b>	0.418	0.173	0.087	0.499	0.746
Linear	0.0130	0.074	0.058	0.068	0.074	0.056	0.535
CellFlow [25]	0.0949	0.205	-0.003	0.110	0.093	-0.033	0.472
Squidiff [30]	4.6410	2.077	0.089	0.039	0.091	0.000	0.432
Mean Variant (per Cell Type)	<u>0.0085</u>	0.057	0.412	0.178	0.087	0.492	0.743
Mean Variant (per Batch)	0.0699	0.174	0.002	0.110	0.092	-0.024	0.475
Mean Variant (Overall)	0.0711	0.175	-0.001	0.111	0.093	-0.027	0.474

As shown in Table 1, SCALE exhibits a clear decoupling between biological accuracy and global expression error. For example, on the PBMC dataset, our model achieves a much higher PDCorr (0.979) and DE Overlap (0.810) than STATE [22] (0.796 and 0.512, respectively). However, it yields a higher MSE (0.0320 vs.  $1.41 \times 10^{-4}$ ).

This divergence is not a flaw, but a direct result of how perturbation responses are modeled and

Table 2 | **Training and inference efficiency of the BioNeMo-based SCALE system.** The table reports training efficiency under each framework’s native epoch definition and inference-oriented throughput under cell-normalized workloads. The training block summarizes native epoch time and iteration throughput, whereas the inference block presents cell-normalized throughput and the corresponding speedup relative to STATE.

Model	Infra	Pretraining			Inference		
		Native epoch time (s) ↓	Iter/s ↑	Speedup vs. STATE (iter/s) ↑	Cells/epoch ↑	Cell-normalized throughput (cells/s) ↑	Speedup vs. STATE (throughput) ↑
STATE-280M	Original	1298.43	0.1540	1.00×	4,705,402	21,584.40	1.00×
SCALE-184M	BioNeMo	<b>243.00</b>	<b>1.9259</b>	<b>12.51×</b>	5,187,584	<b>27,818.20</b>	<b>1.29×</b>

evaluated. We attribute this to three main factors. First, biological perturbations usually affect only a small subset of genes [29]. MSE and MAE calculate errors across all 2,000 highly variable genes evenly. Therefore, a model that slightly shifts the baseline of many unaffected background genes will get a worse MSE, even if it perfectly identifies the crucial differentially expressed genes (DEGs). Second, SCALE learns the perturbation as a transition vector [25]. Metrics like PDCorr evaluate the *direction* and pattern of this change. If the model correctly predicts the direction of gene expression shifts but slightly overestimates the magnitude, the correlation remains very high, even though the absolute distance (MSE) increases. Finally, optimizing strictly for MSE often leads to a "mean-effect" trap [24]. To minimize overall error, baseline models tend to predict a safe, average expression profile. This reduces MSE but smooths out the strong, heterogeneous signals needed to identify true biological responses. Instead of forcing the model to reconstruct an unobserved continuous trajectory or a generic average state, SCALE directly learns the transition between the observed start (control) and end (perturbed) cell populations [22, 24]. This approach avoids the mean-effect trap, prioritizing the recovery of meaningful biological effects over simply fitting an average expression.

**BioNeMo-based training and inference framework for virtual cell perturbation prediction.** To reduce random I/O overhead from large AnnData objects, we preprocess the dataset into LMDB shards organized by experimental condition. Each perturbation sample is stored as a grouped entry together with a sparse matrix block containing all cells under that perturbation, while control cells are stored separately in a dedicated LMDB for efficient retrieval of matched controls during training. Built on top of this storage layout, we implement the full SCALE training stack in BioNeMo to improve distributed execution and end-to-end framework efficiency at SCALE. We also use batch-aware sampling as an auxiliary strategy to improve hardware utilization under highly imbalanced perturbation groups.

Table 2 shows that the dominant finding is end-to-end acceleration from the BioNeMo-based framework. Under each framework’s native epoch definition, SCALE reduces wall-clock epoch time from 1298.43 s to 243.00 s, a 5.34× reduction, and increases raw iteration throughput from 0.1540 to 1.9259 iter/s, yielding a 12.51× gain. Since batch-aware sampling changes the effective number of processed cells per epoch, we additionally report cell-normalized throughput to provide a workload-aligned comparison across frameworks. Under this normalization, SCALE improves effective throughput from 21,584.40 to 27,818.20 cells/s, corresponding to a 1.29× gain over the original STATE pipeline. We emphasize that Table 2 reports end-to-end framework efficiency rather than a component-wise attribution; in particular, dataloader-only speedup is not separately measured here.

**Ablation dimensions.** We perform a systematic ablation study to identify which design choices are responsible for the gains of SCALE. Unless otherwise stated, all ablations are conducted on the 184M-parameter backbone, evaluated on the same validation split, and reported with PDCorr as

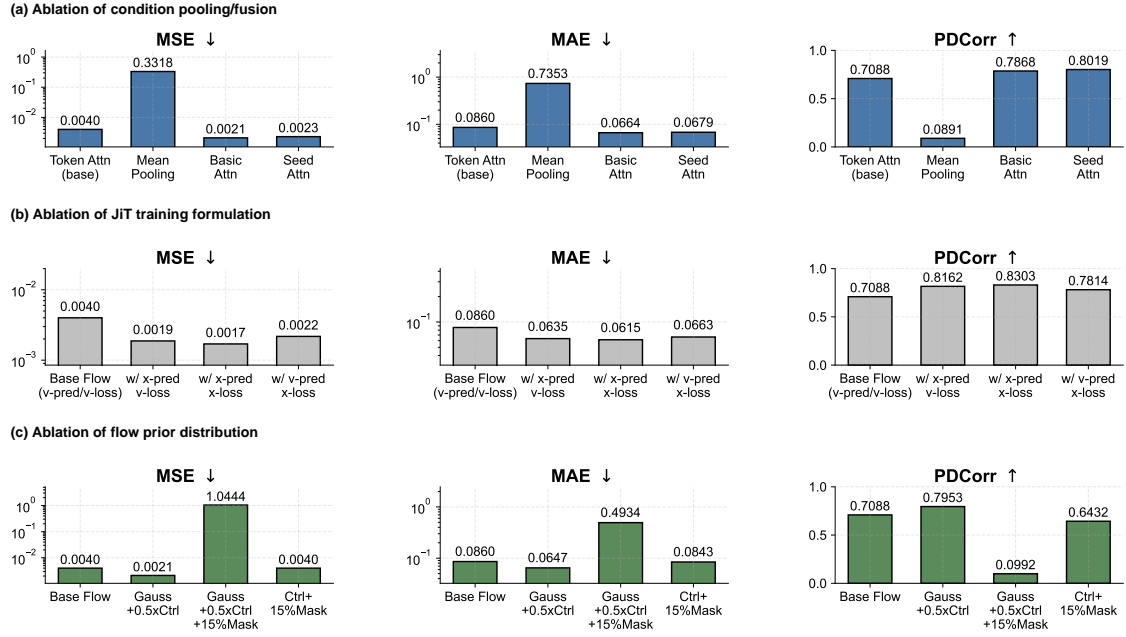


Figure 3 | **Ablation study.** We analyze three key design choices in SCALE: condition pooling/fusion, JiT training formulation, and the design of prior distribution. (a) Adaptive condition aggregation is critical, as mean pooling causes a clear performance drop, while basic and seed attention yield substantially better results. (b) JiT parameterization consistently improves over the base flow formulation, with endpoint-oriented training ( $x$ -pred/ $x$ -loss) achieving the strongest overall performance. (c) A Gaussian-control mixed prior distribution further improves transport learning, whereas masking-based variants severely degrade performance, suggesting that increasing path difficulty can be beneficial but overly destructive corruption is harmful in the latent space.

the primary metric, with MSE and MAE as auxiliary reconstruction metrics. To reduce confounding factors, each ablation changes only one component at a time while keeping the remaining training setup fixed.

We study three orthogonal axes: (1) *condition pooling / fusion method* in the condition encoder, (2) *JiT training formulation* which defines the prediction target and loss space, and (3) *design of prior distribution* for comparison between control-anchored and Gaussian-mixed as the prior distribution. This organization follows the modeling decomposition in the Method Section: condition aggregation determines how heterogeneous perturbation and context cues are compressed, JiT variants determine how the transport target is parameterized, and start-distribution design determines how difficult the learned path is and whether the model is prone to fit a shortcut between the control and perturb data distribution.

**Condition pooling and fusion.** Let  $\{h_i\}_{i=1}^N$  denote token-level condition representations. We write the pooled condition embedding as

$$c = \sum_{i=1}^N \alpha_i h_i, \quad \sum_{i=1}^N \alpha_i = 1, \quad (38)$$

where different fusion backbones correspond to different weighting schemes. Mean pooling uses uniform weights  $\alpha_i = 1/N$ , token attention learns token-wise adaptive weights, and seed attention uses a learnable seed query to aggregate condition tokens. This formulation makes explicit the trade-off

between simplicity and adaptive weighting.

Figure 3(a) shows that condition aggregation is critical. Uniform mean pooling causes a sharp performance drop, reducing PDCorr from 0.7088 to 0.0891, suggesting that naive averaging destroys perturbation-specific signals. Replacing the token-attention baseline with basic attention improves PDCorr to 0.7868, and seed attention further increases it to 0.8019. These results indicate that adaptive aggregation is essential for perturbation prediction, while seed-based aggregation offers a stronger inductive bias than uniform pooling for compressing heterogeneous condition tokens.

**JiT ablation.** We next ablate the JiT formulation by varying both the prediction target and the loss space. Specifically, the model predicts either the latent endpoint  $\hat{Z}_1$  ( $x$ -pred) or the displacement field  $\hat{U}$  ( $v$ -pred), and is trained either in endpoint space ( $x$ -loss) or in displacement space ( $v$ -loss). This yields four possible combinations, among which the baseline Flow corresponds to  $v$ -pred/ $v$ -loss.

As shown in Figure 3(b), all JiT variants outperform the baseline formulation, but the gains are highly asymmetric. The strongest result is obtained by  $x$ -pred/ $x$ -loss, which improves PDCorr from 0.7088 to 0.8303, together with lower MSE and MAE.  $x$ -pred/ $v$ -loss also performs strongly (0.8162), while  $v$ -pred/ $x$ -loss is substantially weaker (0.7814), though still above the baseline. This pattern suggests that, for control-to-perturbation transport in latent space, directly predicting the target endpoint is more stable than predicting an intermediate velocity target derived from interpolation.

A more task-specific interpretation is that many perturbation responses in this benchmark correspond to relatively small and structured displacements from the control state. Under such scenario, learning the final perturbed endpoint may be a better match to the problem geometry than learning a path-wise velocity field along interpolated states. The standard  $v$ -pred formulation requires supervision on intermediate points that are not themselves evaluation targets, and may introduce unnecessary noise or ambiguity when the underlying control-to-perturbed transition is short. By contrast, direct endpoint prediction aligns the optimization objective more closely with the final prediction target. This observation also raises a broader question: **for perturbation regimes dominated by modest state shifts, it is not obvious that a multi-step flow-style formulation is preferable to a simpler end-to-end mapping.** However, we emphasize that flow-based modeling may still provide a stronger inductive bias in regimes with larger state displacements, richer trajectory geometry, or explicit dependence on time, dose, or compositional perturbation structure. In such settings, learning a shared vector field can capture transport regularities beyond a single endpoint and may generalize better than direct endpoint regression.

**Prior distribution design.** We finally examine whether replacing a control-anchored prior distribution with a Gaussian-control mixed initialization can mitigate shortcut behavior. The intuition is that when the start and end states are too similar, the model may overfit trivial shortcuts instead of learning a more general perturbation transport rule. By increasing the discrepancy between the start and target states, the Gaussian-mixed initialization makes the transport problem less degenerate.

The results are summarized in Figure 3(c). Compared with the base Flow model, a Gaussian + 0.5 $\times$  control initialization improves PDCorr from 0.7088 to 0.7953, while also reducing MSE and MAE. This indicates that a partially randomized start can indeed regularize the learning problem and mitigate shortcut behavior. However, masking-based variants do not support a similarly positive conclusion. Applying a 15% mask to the Gaussian-control start causes a severe collapse in performance, and masking the control initialization alone also reduces PDCorr to 0.6432. These observations suggest that random masking in the compressed latent space is too destructive for this task, likely because latent gene representations are already highly compressed and no longer exhibit the kind of sparsity that would make masking benign.

Overall, the start-distribution ablation supports a *qualified* conclusion: increasing path difficulty through Gaussian-control mixing can be beneficial, but masking is not an effective mechanism for improving generalization in the current latent setup.

**Takeaway.** The ablation study reveals that the gains of SCALE do not come from introducing flow matching alone. Instead, they arise from the interaction of three design choices:

**Key Design Principles.** (1) *adaptive condition aggregation*, which is necessary to preserve heterogeneous perturbation cues; (2) *endpoint-oriented JiT parameterization*, which stabilizes optimization in latent transport learning; and (3) *a less degenerate start distribution*, which can reduce shortcut learning when introduced carefully.

Together, these results support the view that large-scale perturbation prediction requires co-design across condition encoding, transport parameterization, and optimization geometry, rather than a single architectural modification.

### 4.3. Scaling Study

We analyze model scaling from a *strict Cell-Eval comparison*, where we evaluate the selected large models using the full h5ad-based cell-level evaluation pipeline on Tahoe validation and test splits.

Table 3 | Scaling study of SCALE under *strict Cell-Eval* on Tahoe using the full h5ad-based evaluation pipeline.

Protocol	Eval Dataset	Params	MSE↓	MAE↓	PDCorr↑	DEOver↑	LFCSpear↑
Strict Cell-Eval	Tahoe val	184M	0.0020	0.0058	0.9589	0.8026	0.8876
Strict Cell-Eval	Tahoe val	280M	0.0020	0.0061	0.9556	0.7975	0.8742
Strict Cell-Eval	Tahoe test	184M	0.0020	0.0058	0.9526	0.8055	0.8758
Strict Cell-Eval	Tahoe test	280M	0.0020	0.0060	0.9502	0.8008	0.8669

**Strict Cell-Eval scaling on Tahoe.** We then examine whether the gains observed in training-time proxy metrics translate into strict biological evaluation. For this purpose, we compare the selected 184M and 280M SCALE models using the full Cell-Eval pipeline on Tahoe *val* and *test*, including not only MSE/MAE/PDCorr but also DE-oriented metrics. Here, the results indicate clear saturation. On Tahoe *val*, the 184M model slightly outperforms the 280M model in PDCorr (0.9589 vs. 0.9556), DE Overlap (0.8026 vs. 0.7975), and DE LFC Spearman (0.8876 vs. 0.8742). The same pattern holds on Tahoe *test*, where the 184M model achieves 0.9526 vs. 0.9502 in PDCorr and 0.8055 vs. 0.8008 in DE Overlap. Although the 280M model remains highly competitive, these results show that under strict biological evaluation, the performance gain saturates around the 184M regime.

**Interpretation.** Taken together, these scaling results suggest a compute-efficient plateau under the current recipe rather than clear evidence for continued biological gains from additional parameter growth. Increasing model capacity is beneficial up to a moderate SCALE in our completed runs, but the strict Cell-Eval results indicate that moving from 184M to 280M does not yield a reliable improvement on the main biological metrics. Practically, this means that, under the present data regime, optimization setup, and evaluation protocol, the 184M model already captures most of the observed benefit while remaining more efficient than the larger 280M alternative.

## 5. Discussion

Our findings motivate a broader re-examination of how virtual-cell perturbation models are evaluated, compared, and interpreted.

**Cell-Eval remains biologically meaningful, but its practical use is still sensitive to implementation details.** Although Cell-Eval is substantially more biologically informative than count-only reconstruction metrics, our results suggest that it is not yet fully stable as an evaluation instrument across codebases and execution paths. In our experiments, reproduced scores can differ across implementations, and training-time proxy metrics do not always agree with the final file-based Cell-Eval results obtained from exported predictions. This implies that benchmark scores may depend not only on model quality, but also on hidden choices in preprocessing, aggregation, serialization, and evaluator code. We therefore believe that future progress in virtual-cell benchmarking will require a more standardized and transparent evaluation pipeline, with stricter control over preprocessing, split construction, perturbation subsets, and evaluator implementation.

**The current flow formulation may be easier to optimize than to generalize.** Second, our ablations raise the possibility that current flow-based perturbation formulations are vulnerable to shortcut solutions. The improvements of our method do not come from flow matching in isolation, but from a specific combination of endpoint-oriented supervision, condition design, and path construction. Notably, the standard control-to-perturbed setup appears easier to optimize than to generalize, especially when the start and target states are already close in representation space. Under such conditions, a model may achieve strong endpoint metrics through local interpolation-friendly heuristics without learning a robust perturbation transport rule. We therefore argue that future work should compare multiple transport-style models under a fully unified setting to determine whether the current flow paradigm captures causal perturbation structure or merely exploits shortcut geometry.

**Cross-paper benchmark comparisons remain only partially protocol-aligned.** Third, many existing comparisons [31–34] remain only partially aligned to the Cell-Eval protocol used by STATE. Prior benchmark tables often combine reproduced baselines with results reported from other works under different preprocessing and evaluation pipelines. Such practice is understandable given the cost of large-scale benchmarking, but it makes small numerical differences difficult to interpret. This problem becomes particularly acute when the evaluator itself is sensitive to implementation details. We therefore believe that strict protocol parity, including identical preprocessing, split construction, perturbation subsets, and evaluator code, is now essential for reliable progress claims.

Likewise, our goal is not to reject flow-based modeling as a whole, but to highlight that the current formulation of control-to-perturbed transport may not yet be the most reliable way to capture perturbation dynamics. We try to suggest that the next bottleneck in virtual-cell prediction may lie less in model scaling alone and more in rebuilding the evaluation and comparison framework around reproducibility, biological validity, and protocol alignment.

## 6. Conclusion

In this work, we have presented SCALE, an endpoint-aligned conditional transport framework for single-cell perturbation prediction under paired endpoint supervision. Rather than attempting to reconstruct an unobserved intermediate biological trajectory, SCALE models perturbation prediction as transport between observed control and perturbed cell populations in a set-aware latent space. This design combines a hierarchical encoder that captures both within-cell transcriptional structure and across-cell population context with a conditional transport backbone that predicts the perturbed endpoint in a tractable and observation-consistent latent representation. Empirically, our results show

that strong performance in virtual-cell prediction depends not only on model capacity, but also on the co-design of scalable infrastructure, endpoint-matched supervision, and biologically grounded evaluation. Taken together, these findings suggest that endpoint-aligned latent transport provides a practical and effective foundation for large-scale virtual-cell modeling across diverse settings.

Overall, **SCALE** provides a simple yet effective view of virtual cell prediction: learn a conditional transport between supervised biological endpoints, anchor the latent manifold to measurable gene expression, and decode the transported state back to expression space for evaluation and downstream analysis. These results suggest that endpoint-aligned latent transport is a promising foundation for scalable perturbation modeling, and may offer a useful path toward more general virtual cell foundation models across datasets, perturbation types, and biological contexts.

## References

- [1] Charlotte Bunne et al. How to build the virtual cell with artificial intelligence: priorities and opportunities. *Cell*, 2024.
- [2] Jennifer E. Rood et al. Toward a foundation model of causal cell and tissue biology with a perturbation cell atlas. *Cell*, 2024.
- [3] Charlotte Bunne et al. Learning single-cell perturbation responses using neural optimal transport. *Nature Methods*, 20:1759–1768, 2023.
- [4] Kenji Kamimoto et al. Dissecting cell identity via network inference and in silico gene perturbation. *Nature*, 2023.
- [5] Yusuf H. Roohani et al. Virtual cell challenge: Toward a turing test for the virtual cell. *Cell*, 2025.
- [6] Tianhong Li and Kaiming He. Back to basics: Let denoising generative models denoise. *arXiv preprint arXiv:2511.13720*, 2025.
- [7] Romain Lopez et al. Deep generative modeling for single-cell transcriptomics. *Nature Methods*, 15:1053–1058, 2018.
- [8] Haotian Cui, Chloe Wang, Hassaan Maan, Kuan Pang, Fei Luo, Nan Duan, and et al. scgpt: toward building a foundation model for single-cell multi-omics using generative ai. *Nature Methods*, 21(8):1470–1480, 2024. doi: 10.1038/s41592-024-02201-0. URL <https://pubmed.ncbi.nlm.nih.gov/38409223/>.
- [9] Gefei Wang, Tianyu Liu, Jia Zhao, Youshu Cheng, and Hongyu Zhao. Modeling and predicting single-cell multi-gene perturbation responses with sclambda. *Bioinformatics*, 2024.
- [10] Mohammad Lotfollahi, F. Alexander Wolf, and Fabian J. Theis. scgen predicts single-cell perturbation responses. *Nature Methods*, 16(8):715–721, 2019. doi: 10.1038/s41592-019-0494-8. URL <https://www.nature.com/articles/s41592-019-0494-8>.
- [11] Mohammad Lotfollahi et al. Predicting cellular responses to complex perturbations in high-throughput screens. *Molecular Systems Biology*, 19(6):e11517, 2023. doi: 10.15252/msb.202211517. URL <https://pubmed.ncbi.nlm.nih.gov/37154091/>.
- [12] Yusuf Roohani, Kexin Huang, and Jure Leskovec. Predicting transcriptional outcomes of novel multigene perturbations with gears. *Nature Biotechnology*, 2024. doi: 10.1038/s41587-023-01905-6. URL <https://www.nature.com/articles/s41587-023-01905-6>.

- 
- [13] Ke Wei et al. scpregan: a generative adversarial network for single-cell perturbation prediction. *Bioinformatics*, 38(13):3377–3385, 2022.
- [14] Qun Jiang, Shengquan Chen, Xiaoyang Chen, and Rui Jiang. scpram accurately predicts single-cell gene expression perturbation response based on attention mechanism. *Bioinformatics*, 40(5):bt265, 2024. doi: 10.1093/bioinformatics/bt265.
- [15] Constantin Ahlmann-Eltze, Wolfgang Huber, and Simon Anders. Deep-learning-based gene perturbation effect prediction does not yet outperform simple linear baselines. *Nature Methods*, 22(8):1657–1661, 2025. doi: 10.1038/s41592-025-02772-6. URL <https://pubmed.ncbi.nlm.nih.gov/40759747/>.
- [16] Charlotte Bunne, Stefan G. Stark, Gabriele Gut, and et al. Learning single-cell perturbation responses using neural optimal transport. *Nature Methods*, 20(11):1759–1768, 2023. doi: 10.1038/s41592-023-01969-x. URL <https://www.nature.com/articles/s41592-023-01969-x>.
- [17] Alexander Tong et al. Cinema-ot: causal inference of single-cell perturbation effects via optimal transport. *Nature Methods*, 2023.
- [18] Zhen Yao et al. Perturbnet: Learning single-cell perturbation responses with graph neural networks. In *NeurIPS*, 2022.
- [19] et al. Wang. screpa: representation learning for single-cell perturbation analysis. *Briefings in Bioinformatics*, 2025.
- [20] Kang Bioinformatics Lab. Inferring perturbation responses in temporally sampled single-cell data. *Briefings in Bioinformatics*, 23(5), 2022.
- [21] Chenglei Yu, Chuanrui Wang, Bangyan Liao, and Tailin Wu. scdfm: Distributional flow matching model for robust single-cell perturbation prediction. *arXiv preprint arXiv:2602.07103*, 2026.
- [22] Abhinav K. Adduri, Dhruv Gautam, Beatrice Bevilacqua, Alishba Imran, Rohan Shah, et al. Predicting cellular responses to perturbation across diverse contexts with State. *bioRxiv*, 2025. doi: 10.1101/2025.06.26.661135. URL <https://www.biorxiv.org/content/10.1101/2025.06.26.661135v2>.
- [23] Zhaokang Liang et al. scppdm: A diffusion model for single-cell drug-response prediction. *arXiv preprint arXiv:2510.11726*, 2025.
- [24] Xinyu Yuan, Xixian Liu, Ya Shi Zhang, Zuobai Zhang, Hongyu Guo, and Jian Tang. Perturbdiff: Functional diffusion for single-cell perturbation modeling, 2026. URL <https://arxiv.org/abs/2602.19685>.
- [25] Dominik Klein, Jonas Simon Fleck, Daniil Bobrovskiy, Lea Zimmermann, Sören Becker, et al. CellFlow enables generative single-cell phenotype modeling with flow matching. *bioRxiv*, 2025. doi: 10.1101/2025.04.11.648220. URL <https://www.biorxiv.org/content/10.1101/2025.04.11.648220v1>.
- [26] Changxi Chi, Jun Xia, Yufei Huang, Jingbo Zhou, Siyuan Li, Yunfan Liu, Chang Yu, and Stan Z. Li. Unlasting: Unpaired single-cell multi-perturbation estimation by dual conditional diffusion implicit bridges, 2025. URL <https://arxiv.org/abs/2506.21107>.
-

- 
- [27] Jesse Zhang, Airol A. Ubas, Richard de Borja, Valentine Svensson, Nicole Thomas, Neha Thakar, Ian Lai, Aidan Winters, Umair Khan, Matthew G. Jones, et al. Tahoe-100m: A giga-scale single-cell perturbation atlas for context-dependent gene function and cellular modeling. *bioRxiv*, 2025. doi: 10.1101/2025.02.20.639398.
- [28] Joseph M. Replogle, Reuben A. Saunders, Angela N. Pogson, Jeffrey A. Hussmann, Alexander Lenail, Aleksandra Guna, Laura Mascibroda, Emily J. Wagner, Kyuho Adelman, Galia Lithwick-Yanai, et al. Mapping information-rich genotype-phenotype landscapes with genome-scale perturb-seq. *Cell*, 185(14):2559–2575.e28, 2022. doi: 10.1016/j.cell.2022.05.013.
- [29] Ajay Nadig, Joseph M. Replogle, Angela N. Pogson, Mukundh Murthy, Steven A. McCarroll, Jonathan S. Weissman, Elise B. Robinson, and Luke J. O’Connor. Transcriptome-wide analysis of differential expression in perturbation atlases. *Nature Genetics*, 57(5):1228–1237, 2025. doi: 10.1038/s41588-025-02169-3.
- [30] Siyu He, Yuefei Zhu, Daniel Naveed Tavakol, Haotian Ye, Yeh-Hsing Lao, Zixian Zhu, Cong Xu, Shradha Chauhan, Guy Garty, Raju Tomer, Gordana Vunjak-Novakovic, James Zou, Elham Azizi, and Kam W. Leong. Squidiff: predicting cellular development and responses to perturbations using a diffusion model. *Nature Methods*, 23(1):65–77, 2026. doi: 10.1038/s41592-025-02877-y. URL <https://www.nature.com/articles/s41592-025-02877-y>.
- [31] Y. Wu et al. Perturbench: Benchmarking machine learning models for single-cell perturbation prediction. *arXiv preprint arXiv:2408.10609*, 2024.
- [32] A systematic comparison of single-cell perturbation response prediction models. *bioRxiv*, 2025.
- [33] BM2 Lab. Benchmarking algorithms for generalizable single-cell perturbation prediction. <https://bm2-lab.github.io/scPerturBench-reproducibility/>, 2024.
- [34] A benchmark for prediction of transcriptomic responses to perturbations. In *NeurIPS*, 2024.

## A. Perturbation Metrics

We adopt the evaluation protocol used in CellFlow [25] and the Cell-Eval framework (version 0.6.6) from STATE to assess perturbation prediction performance. A fundamental challenge in single-cell perturbation prediction is that individual cells cannot be matched to a specific ground truth due to biological variability and the destructive nature of sequencing. Therefore, evaluation must rely on statistics computed at the population level.

For clarity, the evaluation metrics are organized along two axes.

**Cell-level evaluation.** These metrics quantify expression-level fidelity by comparing statistical summaries between predicted cell populations and the corresponding ground-truth populations.

**Gene-level evaluation.** These metrics assess biological signal consistency by examining whether predicted perturbation responses recover the differential expression patterns observed in the ground truth.

To ensure fair comparison across methods, the same set of control cells is used when computing both predicted and ground-truth statistics. As a result, performance differences reflect only the quality of the predicted perturbed-cell responses.

**Notation.** Let  $M$  denote the total number of perturbation conditions. For a perturbation  $\lambda$ , let  $\{\mathbf{x}_{\lambda,i}^{\text{pert}}\}_{i=1}^{N_{\text{pert}}^{\lambda}}$  and  $\{\mathbf{x}_{\lambda,i}^{\text{ctrl}}\}_{i=1}^{N_{\text{ctrl}}^{\lambda}}$  denote the ground-truth expression profiles of perturbed and control cells. Let  $\{\hat{\mathbf{x}}_{\lambda,i}^{\text{pert}}\}_{i=1}^{N_{\text{pert}}^{\lambda}}$  denote the predicted perturbed cells. In practice, Cell-Eval uses  $N_{\text{ctrl}}^{\lambda} = N_{\text{pert}}^{\lambda}$ .

We define pseudobulk expression profiles as the mean expression across cells:

$$\bar{\mathbf{x}}_{\lambda}^{\text{pert}} = \frac{1}{N_{\text{pert}}^{\lambda}} \sum_{i=1}^{N_{\text{pert}}^{\lambda}} \mathbf{x}_{\lambda,i}^{\text{pert}}, \quad \bar{\mathbf{x}}_{\lambda}^{\text{ctrl}} = \frac{1}{N_{\text{ctrl}}^{\lambda}} \sum_{i=1}^{N_{\text{ctrl}}^{\lambda}} \mathbf{x}_{\lambda,i}^{\text{ctrl}}. \quad (39)$$

The pseudobulk profile for predicted perturbed cells is

$$\bar{\hat{\mathbf{x}}}_{\lambda}^{\text{pert}} = \frac{1}{N_{\text{pert}}^{\lambda}} \sum_{i=1}^{N_{\text{pert}}^{\lambda}} \hat{\mathbf{x}}_{\lambda,i}^{\text{pert}}. \quad (40)$$

The **relative perturbation effect** is defined as the difference between perturbed and control pseudobulk profiles:

$$\Delta \mathbf{x}_{\lambda} = \bar{\mathbf{x}}_{\lambda}^{\text{pert}} - \bar{\mathbf{x}}_{\lambda}^{\text{ctrl}}, \quad (41)$$

$$\Delta \hat{\mathbf{x}}_{\lambda} = \bar{\hat{\mathbf{x}}}_{\lambda}^{\text{pert}} - \bar{\mathbf{x}}_{\lambda}^{\text{ctrl}}. \quad (42)$$

These quantities are used throughout the evaluation metrics below.

### A.0.1. Averaged Expression Accuracy

- **Coefficient of Determination ( $R^2$ ).** The  $R^2$  metric measures the fraction of variance in the ground-truth data explained by the predictions relative to the empirical mean baseline:

$$R^2 = 1 - \frac{\sum_i (y_i - \hat{y}_i)^2}{\sum_i (y_i - \bar{y})^2}.$$

Higher values indicate better predictive accuracy.

- **Perturbation Discrimination Score (PDS)**. PDS evaluates whether the predicted perturbation profile is closest to its own ground truth compared with other perturbations:

$$\text{PDS} = 1 - \frac{1}{M} \sum_{\lambda=1}^M \frac{r_\lambda}{M}, \quad r_\lambda = \sum_{p \neq \lambda} \mathbb{1} [d(\Delta \hat{\mathbf{x}}_\lambda, \Delta \mathbf{x}_p) < d(\Delta \hat{\mathbf{x}}_\lambda, \Delta \mathbf{x}_\lambda)].$$

A value of 1 indicates perfect discrimination, while a value close to 0.5 corresponds to random performance. We report three variants using different distance functions: L1 distance ( $\text{PDS}_{\text{L1}}$ ), L2 distance ( $\text{PDS}_{\text{L2}}$ ), and cosine distance ( $\text{PDS}_{\text{cos}}$ ).

- **Pearson Delta Correlation (PDCorr)**. For each perturbation  $\lambda$ , the Pearson correlation between predicted and ground-truth perturbation effects is computed as

$$\text{PDCorr} = \frac{1}{M} \sum_{\lambda=1}^M \text{PearsonR}(\Delta \hat{\mathbf{x}}_\lambda, \Delta \mathbf{x}_\lambda).$$

- **Mean Absolute Error (MAE)**. MAE measures the discrepancy between predicted and ground-truth perturbation effects:

$$\text{MAE} = \frac{1}{M} \sum_{\lambda=1}^M \|\Delta \hat{\mathbf{x}}_\lambda - \Delta \mathbf{x}_\lambda\|_1.$$

- **Mean Squared Error (MSE)**. MSE penalizes larger deviations more strongly by using the squared Euclidean distance:

$$\text{MSE} = \frac{1}{M} \sum_{\lambda=1}^M \|\Delta \hat{\mathbf{x}}_\lambda - \Delta \mathbf{x}_\lambda\|_2^2.$$

### A.0.2. Biologically Meaningful Differential Patterns

To assess biological relevance, Cell-Eval performs differential expression (DE) analysis using the Wilcoxon rank-sum test. To control false discoveries arising from multiple testing across thousands of genes,  $p$ -values are adjusted using the Benjamini–Hochberg procedure, which controls the false discovery rate (FDR). DE analysis is performed independently on ground-truth cells and predicted cells.

**Notation related to DEGs.** Let  $\mathcal{G}$  denote the set of the top 2,000 highly variable genes (HVGs) used in perturbation prediction. For perturbation  $\lambda$ , a gene  $g \in \mathcal{G}$  is considered significantly differentially expressed if its adjusted  $p$ -value satisfies  $p_{\text{adj}} < 0.05$ .

Let  $\mathcal{G}_\lambda^{\text{DE}}$  denote the set of significant DE genes in the ground truth and  $\hat{\mathcal{G}}_\lambda^{\text{DE}}$  the corresponding set from predicted cells.

Genes are ranked by absolute log-fold change:

$$|\log \text{FC}_{\lambda,g}| = \left| \log_2 \frac{\bar{\mathbf{x}}_{\lambda,g}^{\text{pert}} + \epsilon}{\bar{\mathbf{x}}_{\lambda,g}^{\text{ctrl}} + \epsilon} \right|.$$

Predicted fold changes are computed analogously using predicted pseudobulk expressions. Let  $\mathcal{G}_\lambda^k$  and  $\hat{\mathcal{G}}_\lambda^k$  denote the top- $k$  ranked DE genes from ground-truth and predicted cells.

- **DE Overlap (DEOver).**

$$\text{DEOver}_k = \frac{1}{M} \sum_{\lambda=1}^M \frac{|\mathcal{G}_\lambda^k \cap \hat{\mathcal{G}}_\lambda^k|}{k}.$$

Here  $k = |\mathcal{G}_\lambda^{\text{DE}}|$ .

- **DE Precision (DEPrec).**

$$\text{DEPrec}_k = \frac{1}{M} \sum_{\lambda=1}^M \frac{|\mathcal{G}_\lambda^k \cap \hat{\mathcal{G}}_\lambda^k|}{|\hat{\mathcal{G}}_\lambda^k|}.$$

Here  $k = |\hat{\mathcal{G}}_\lambda^{\text{DE}}|$ .

- **Direction Agreement (DirAgr).** Let

$$\mathcal{G}_\lambda^\cap = \hat{\mathcal{G}}_\lambda^{\text{DE}} \cap \mathcal{G}_\lambda^{\text{DE}}.$$

$$\text{DirAgr} = \frac{1}{M} \sum_{\lambda=1}^M \frac{|\{g \in \mathcal{G}_\lambda^\cap : \text{sgn}(\widehat{\log \text{FC}}_{\lambda,g}) = \text{sgn}(\log \text{FC}_{\lambda,g})\}|}{|\mathcal{G}_\lambda^\cap|}.$$

- **Log Fold-change Spearman Correlation (LFCspear).**

$$\text{LFCspear} = \frac{1}{M} \sum_{\lambda=1}^M \text{SpearmanR} \left( (\log \text{FC}_{\lambda,g})_{g \in \mathcal{G}_\lambda^{\text{DE}}}, (\widehat{\log \text{FC}}_{\lambda,g})_{g \in \mathcal{G}_\lambda^{\text{DE}}} \right).$$

- **ROC-AUC (AUROC).**

Genes in  $\mathcal{G}_\lambda^{\text{DE}}$  are treated as positives and the remaining genes as negatives. Predicted significance scores are defined as the negative log-transformed adjusted  $p$ -values. AUROC is computed for each perturbation and averaged across perturbations.

- **PR-AUC (AUPRC).**

This metric is computed analogously to AUROC but summarizes the precision–recall trade-off instead of the ROC curve.